Multi-patch isogeometric neural solver for partial differential equations on computer-aided design domains

Moritz von Tresckow^{1†}, Ion Gabriel Ion^{2†}, Dimitrios Loukrezis^{3*}

¹Institute for Accelerator Science and Electromagnetic Fields, Technische Universität Darmstadt, Schlossgartenstr. 8, Darmstadt, 64289, Germany.
²Terra Quantum AG, Kornhausstr. 25, St. Gallen, 9000, Switzerland.
^{3*}Scientific Computing, Centrum Wiskunde & Informatica, Science Park 123, Amsterdam, 1098 XG, The Netherlands.

*Corresponding author(s). E-mail(s): d.loukrezis@cwi.nl; Contributing authors: moritz.von_tresckow@tu-darmstadt.de; igi@terraquantum.swiss;

[†]These authors contributed equally to this work.

Abstract

This work develops a computational framework that combines physics-informed neural networks with multi-patch isogeometric analysis to solve partial differential equations on complex computer-aided design geometries. The method utilizes patch-local neural networks that operate on the reference domain of isogeometric analysis. A custom output layer enables the strong imposition of Dirichlet boundary conditions. Solution conformity across interfaces between non-uniform rational B-spline patches is enforced using dedicated interface neural networks. Training is performed using the variational framework by minimizing the energy functional derived after the weak form of the partial differential equation. The effectiveness of the suggested method is demonstrated on two highly non-trivial and practically relevant use-cases, namely, a 2D magnetostatics model of a quadrupole magnet and a 3D nonlinear solid and contact mechanics model of a mechanical holder. The results show excellent agreement to reference solutions obtained with high-fidelity finite element solvers, thus highlighting the potential of the suggested neural solver to tackle complex engineering problems given the corresponding computer-aided design models.

1 Introduction

1.1 Motivation

In recent years, physics-informed neural networks (PINNs) [1] have emerged as a possible mesh-free alternative to traditional, mesh-based numerical methods for the solution of partial differential equations (PDEs). Within the PINN framework, neural networks (NNs) are trained to learn a PDE solution by minimizing a loss function which incorporates the boundary value problem (BVP) that describes the underlying physics of the system under investigation [2, 3]. It must be noted that methods based on very similar ideas were developed prior to the seminal PINN paper, such as the deep Ritz and deep Galerkin methods [4, 5]. However, PINN has been established as a blanket term for most related approaches and is used as such within this paper as well.

The PINN framework and its numerous variants [6–10] have already found applications in several fields of computational science and engineering, as in computational electromagnetics [11–14], fluid dynamics [15–18], and mechanics [19–22], to name only a few indicative application areas. Nonetheless, due to a number of weaknesses, PINNs cannot yet be regarded as competitive to traditional numerical solvers [23, 24]. This work focuses on the severe difficulties that PINNs face when applied to complex domains, in particular shapes and geometries stemming from computer-aided design (CAD). In turn, these difficulties hinder the application of PINNs to real-world engineering problems, where complex, multi-patch CAD geometries are ubiquitous.

In this context, three main challenges remain largely unaddressed. The first challenge concerns the enforcement of solution conformity across complex, multi-patch domains. Solution continuity in particular is crucial when dealing with different materials across domain interfaces. The second challenge concerns the imposition of Dirichlet boundary conditions (BCs). The standard PINN framework and most related approaches use a soft-constraints approach, such that the PINN learns the BCs during training. However, in many settings, the BCs must be strongly conformed to. The third challenge concerns handling geometry parts with significant variations in size and shape. Such differences make data normalization difficult, especially under physical conformity requirements.

1.2 Contribution

This work aims to enable the application of PINNs to CAD geometries by addressing the three aforementioned limitations. Of particular interest are complex, multi-patch CAD geometries, which are rarely addressed in the relevant literature. To that end, we introduce a novel neural solver which combines PINNs with isogeometric analysis (IGA) [25–27]. More specifically, the neural solver developed in this work is rooted in the finite element tearing and interconnecting (FETI) method [28] and its extension

to IGA [29], as well as on mortaring methods [30–32]. Therein, the PINN framework is integrated.

Our approach consists of developing NN-based ansatz functions that approximate the PDE solution by operating on the reference domain of IGA. The solution on the physical domain is obtained by using the pushforward map from the reference to the physical domain, as given by the non-uniform rational B-spline (NURBS)-based parametrization of the geometry, similar to the conventional IGA. The suggested ansatz functions also satisfy Dirichlet BCs where necessary, ensure differentiability within the subdomains (patches) of the physical geometry, and ensure solution continuity across patches.

One set of ansatz functions is used to approximate the PDE solution within the reference domain of each individual patch, thereby leveraging the geometric accuracy of IGA. The output layer of these NNs is modified to strongly impose the Dirichlet boundary conditions where necessary. Another set of ansatz functions is defined on the interfaces between neighboring patches, which appropriately connect the solutions of the individual patches, thus ensuring solution conformity across them. Training is performed by utilizing the variational PINN framework [4, 7, 33], where the loss function to be minimized is the discretized energy functional derived after the weak form of the PDE. This is a natural choice, as it aligns with the principles of IGA, which is also built upon variational formulations.

The suggested neural solver offers three distinct contributions, each connected to one of the challenges identified above. First, it ensures control over solution continuity across patch interfaces. Second, it enables the strong imposition of Dirichlet BCs. Third, by operating on the reference domain, it naturally normalizes NN inputs. The efficacy of the method is demonstrated on two real-world engineering applications. The first use-case is drawn from the field of computational electromagnetics and concerns a 2D magnetostatics model of a quadrupole magnet. The second use-case is drawn from the field of computational mechanics and concerns a 3D nonlinear solid mechanics model of a mechanical holder. For the latter, we employ a hyperelastic material model combined with contact BCs and introduce parametric dependencies in the solution.

1.3 Related work

Prior works have explored the combination of NNs and PINNs with IGA, e.g., for applications in solid mechanics [34–36] or electromagnetics [37, 38], including IGA variants such as isogeometric collocation methods [39] and the isogeometric boundary element method [38]. Differentiable NURBS [40] were developed as a means to integrate CAD models into deep learning frameworks. Isogeometric NNs [41] combine NURBS with NNs to predict NURBS coefficients and approximate PDE solutions for varying physical and geometric parameters. Deep NNs have been used to determine the optimum number of quadrature points for evaluating IGA stifness matrices [42]. The deep NURBS method [43] introduces an ansatz for boundary-conforming NNs. Graph NNs have been employed to learn the PDE solution at the control points of splines [44, 45], while convolutional NNs have also been used in a similar context [46–49]. However, most, if not all, of these related works concern single-patch geometries. Hence, their application for complex, multi-patch domains is not straightforward. For

the same reason, solution conformity across interfaces is rarely a concern. One exception is the work of von Tresckow et al. [37], which does consider multi-patch CAD geometries and introduces a discontinuous Galerkin-based PINN formulation to weakly impose interface conditions and Dirichlet BCs. The approach developed in this work is substantially different.

In relation to solution conformity across interfaces, prior works have combined PINNs with domain decomposition methods, using different strategies such as physics-based coupling terms [50, 51], network combinations [52], or tailored NN architectures [53]. In contrast to the present work, these methods are not applied in the context of CAD and consider relatively simple computational domains. Additionally, the present work assigns interface-specific NNs to enforce the correct solution continuity, which is a new approach, at least to the knowledge of the authors.

Concerning the imposition of Dirichlet BCs, most approaches based on the PINN framework enforce BCs only weakly, by incorporating them into the loss function. A few works have considered the exact imposition of Dirichlet BCs, mainly by means of dedicated distance functions [54, 55]. In contrast, our method employs a custom output layer with residual connection as part of the NN-based ansatz functions, which is responsible for the strong enforcement of Dirichlet BCs.

To overcome limitations related to large variations in the data, normalization has been attempted also in the context of PINNs and other neural solvers. Specific examples include the use of scaling factors [56], hierarchical normalization [57], dynamic normalization [58], normalization by non-dimensionalization [59], and variable linear transformation [60]. A disadvantage shared by these approaches is that the normalization procedure must be derived anew for each specific problem. Contrarily, normalization is performed naturally within our method, as it operates on the reference domain of IGA.

1.4 Paper organization

The remaining of this paper is organized as follows. In section 2, we recall the variational PINN framework, which concerns the use of NNs to solve energy functional minimization problems arising from variational PDE formulations. In section 3, we recall some fundamental tools of CAD and IGA, to be used throughout the paper. Section 4 presents the core methodological contribution of this work, that is, the construction of NN-based ansatz functions tailored for multi-patch CAD domains, as well as the complete neural solver. In section 5, our method is applied to two practical use-cases, namely, a 2D magnetostatics simulation of a quadrupole magnet and a 3D solid and contact mechanics simulation of a mechanical holder. For each use-case, we outline the theoretical formulation for the particular problem at hand, followed by a comprehensive presentation of the numerical results. Last, section 6 summarizes the findings of this work and discusses follow-up research possibilities.

2 Variational physics-informed neural networks

We focus on elliptic BVPs, for which energy functional formulations exist. This choice is motivated by the fact that the energy formulation provides a natural optimization setting aligned with NN training. Additionally, it avoids computing higher order derivatives, which can oftentimes be problematic [5].

As solution function, we assume a scalar-field state, $u:\Omega\to\mathbb{R}$, where $\Omega\subset\mathbb{R}^d$, $d\in\{1,2,3\}$, denotes the computational domain. Typically, there is no general rule for the existence of energy functionals. An elliptic differential equation in particular admits an energy functional if and only if it is the Euler-Lagrange equation of a variational problem [61]. This means that the equation can be derived as the condition for a critical point (typically a minimum) of some functional, which usually takes the form

$$I(u) = \int_{\Omega} L(\mathbf{x}, u, \mathbf{grad}u) \, d\mathbf{x}, \tag{1}$$

where L is a function, typically referred to as the Lagrangian of the associated problem. The solution function needs to fulfill the Euler-Lagrange equation, which for a scalar-field state u reads

$$\frac{\partial L}{\partial u} - \operatorname{div}\left(\frac{\partial L}{\partial \left(\mathbf{grad}u\right)}\right) = 0. \tag{2}$$

Solving the Euler-Lagrange equation (2) is equivalent to minimizing the energy functional (1). The system's equilibrium state, u^* , is obtained as the result of this minimization problem, such that

$$u^* = \operatorname*{argmin}_{u \in \mathcal{V}} I(u), \tag{3}$$

where \mathcal{V} is a function space containing all functions that satisfy the necessary regularity conditions and BCs of the BVP at hand. The Lagrangian exists for many elliptic PDEs, including the use-cases considered in section 5. The specific energy functional minimization formulations are derived in sections 5.1 and 5.2, respectively. For the same use-cases, \mathcal{V} is the Sobolev space $H^1(\Omega) = \{u \in L^2 : \mathbf{grad}u \in L^2(\Omega)\}$. Accordingly, u^* is the solution to the corresponding BVP.

Utilizing the variational PINN framework [4, 7, 33], the trial functions $u \in \mathcal{V}$ are approximated by an NN. We denote this approximation as $u_{\theta} \approx u$, where $\theta \in \Theta$ is a vector containing the NN's trainable parameters and Θ denotes the corresponding parameter space. Feedforward NNs are used in the following. Assuming an NN with L layers and n_l neurons in the l-th layer, $l = 1, \ldots, L$, the trainable parameter vector is given as $\theta = \{\mathbf{W}_l, \mathbf{b}_l\}_{l=1}^L$, where $\mathbf{W}_l \in \mathbb{R}^{n_{l-1} \times n_l}$ and $\mathbf{b}_l \in \mathbb{R}^{n_l}$ are the l-th layer's weight matrix and bias vector, respectively. For consistency of notation, the input vector has size n_0 . Substituting u with u_{θ} in (3), the NN that best approximates the equilibrium state and, accordingly, the solution to the BVP, is the one with the

$$\boldsymbol{\theta}^* = \operatorname*{argmin}_{\boldsymbol{\theta} \in \Theta} I\left(u_{\boldsymbol{\theta}}\right). \tag{4}$$

Note that, in order to have a well-defined problem, the essential BCs must be embedded into the structure of the NN. That is, u_{θ} must fulfill the essential BCs for all $\theta \in \Theta$. This will be further discussed in section 4.1.

From the above, it is obvious that the energy functional is the natural loss function to be minimized during NN training, in order to compute the optimal parameter vector θ^* . This is accomplished by first discretizing the energy functional, typically by means of numerical quadrature [4, 5, 7], and then using a gradient-based optimization method, typically a variant of stochastic gradient descent [62, 63]. The solution of the resulting nonlinear optimization problem yields the set of optimal parameters, i.e., the ones that minimize the discrete energy functional.

3 Computer-aided design and isogeometric analysis

3.1 Non-uniform rational B-spline

NURBS is the central mathematical tool in CAD, which provides mathematical representations for modeling curves, surfaces, and volumes [64]. NURBS offers the flexibility and precision needed to represent both simple geometric shapes and complex freeform objects, as it can accurately model both standard analytic forms and arbitrary shapes defined by control points.

The NURBS parametrization is defined over a d-dimensional reference domain, commonly called the pre-image and here denoted as $\hat{\Omega} = [-1,1]^d$, with its image representing the computational domain $\Omega \subset \mathbb{R}^d$. For $\hat{\mathbf{x}} \in \hat{\Omega}$, the NURBS parametrization is expressed as

$$f(\hat{\mathbf{x}}) = \sum_{i_1, \dots, i_d = 1}^{n_1, \dots, n_d} \mathbf{p}_{i_1, \dots, i_d} \frac{w_{i_1, \dots, i_d} b_{i_1}^{(1)}(\hat{x}_1) \cdots b_{i_d}^{(d)}(\hat{x}_d)}{\sum_{j_1, \dots, j_d = 1}^{n_1, \dots, n_d} w_{j_1, \dots, j_d} b_{j_1}^{(1)}(\hat{x}_1) \cdots b_{j_d}^{(d)}(\hat{x}_d)},$$
(5)

such that $\boldsymbol{f}: \hat{\Omega} \to \Omega$, where $\mathbf{p}_{i_1,\dots,i_d} \in \Omega$ are control points, w_{i_1,\dots,i_d} are the corresponding weights, and $\left\{b_{i_k}^{(k)}\right\}_{i=1}^{n_k}$, $k=1,\dots,d$, is a basis consisting of univariate B-spline basis functions defined by the Cox–de-Boor formula. Note that, for non-self-penetrating domains Ω , \boldsymbol{f} is a bijective map, equivalently, \boldsymbol{f}^{-1} exists and is differentiable.

3.2 Pushforward and pullback operators

The core concept of IGA is to use NURBS as basis functions for the numerical solution of PDEs, essentially integrating CAD tools into the finite element method (FEM). Utilizing the NURBS parametrization, f, the solution of the PDE is first represented on the reference domain and then mapped onto the physical domain.

Similar to section 2, scalar-field solutions are assumed in both the physical and the reference domain, respectively denoted as $u: \Omega \to \mathbb{R}$ and $\hat{u}: \hat{\Omega} \to \mathbb{R}$. Then, the

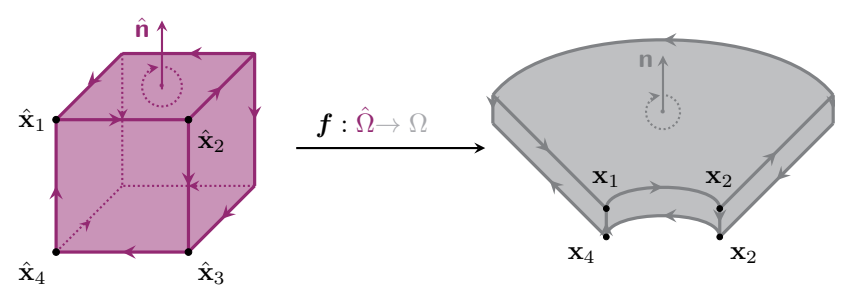


Fig. 1: Illustration of the NURBS-based geometry map from the reference to the physical domain. We have $\mathbf{x}_k = f(\hat{\mathbf{x}}_k), k = 1, ..., 4$. The normal $\hat{\mathbf{n}}$ is transformed to \mathbf{n} .

pushforward operation maps the solution from the reference to the physical domain, and is defined as

$$u = \mathbf{f}_* \hat{u} = \hat{u} \circ \mathbf{f}^{-1}, \tag{6}$$

such that $f_*: \hat{\Omega} \to \Omega$, where the symbol \circ denotes function composition. The inverse pullback operation transforms the solution back to the reference domain, and is defined as

$$\hat{u} = \mathbf{f}^* u = u \circ \mathbf{f},\tag{7}$$

such that $f^*: \Omega \to \hat{\Omega}$.

Using the integral transformation rule to express the energy functional as an integral over the reference domain and integrating the scalar function u in the physical domain leads to

$$\int_{\Omega} u(\mathbf{x}) d\mathbf{x} = \int_{\hat{\Omega}} \hat{u}(\hat{\mathbf{x}}) |\det(\partial \mathbf{f})| d\hat{\mathbf{x}},$$
(8)

where $\partial \mathbf{f}$ denotes the Jacobian of the NURBS parametrization. The following transformations hold for the gradient and the surface normal:

$$\mathbf{grad} \ u = (\partial \mathbf{f})^{-\top} \mathbf{grad} \ \hat{u},$$
$$\mathbf{n} = |\det(\partial \mathbf{f})|(\partial \mathbf{f})^{-\top} \hat{\mathbf{n}},$$
(9)

where **grad** \hat{u} is the gradient expressed in reference domain coordinates and $\hat{\mathbf{n}}$ is the outer normal on the boundary of the reference domain. Figure 1 presents an explanatory illustration.

Note that the pushforward and pullback operations defined in equations (6) and (7), respectively, hold for scalar fields only. However, in certain cases, they can be applied element-wise to the components of a vector field. One such example is considered in the numerical use-case presented in section 5.2.

3.3 Multi-patch CAD geometries

A single NURBS has only limited ability to represent a wide variety of shapes, thus making it unsuitable for parametrizing arbitrary, non-trivial CAD domains.

Consequently, multiple NURBS parametrizations are required, each parametrizing a subdomain of the geometry. Collectively, these subdomains form the physical geometry. In the following, the term "patch" is used interchangeably for both a subdomain of the physical geometry and its corresponding NURBS parametrization.

We assume N_{Ω} NURBS parametrizations, denoted as $\boldsymbol{f}_i, i=1,\ldots,N_{\Omega}$, each representing a subdomain $\Omega_i\subset\Omega$. To construct a multi-patch geometry, the individual patches are generated by mapping a reference domain $\hat{\Omega}_i=[-1,1]^d$ onto the physical geometry, such that $\boldsymbol{f}_i\left(\hat{\Omega}_i\right)=\Omega_i$. This mapping ensures that the collection $\{\Omega_i\}_{i=1}^{N_{\Omega}}$ forms a domain decomposition, such that $\Omega=\bigcup_{i=1}^{N_{\Omega}}\Omega_i$. Note that, although the reference domains $\hat{\Omega}:=\hat{\Omega}_1=\cdots=\hat{\Omega}_{N_{\Omega}}=[-1,1]^d$ are identical, individual indexing is necessary, because the points $\hat{\mathbf{x}}\in\hat{\Omega}_i$ are mapped differently onto Ω , depending on the patch-specific NURBS parametrization \boldsymbol{f}_i .

In this work, the patches are assumed to be non-overlapping and conforming at their interfaces. Non-overlapping means that the interiors of the patches are mutually disjoint. Denoting the boundary of a subdomain Ω_i as $\partial\Omega_i$, this means that $(\Omega_i \setminus \partial\Omega_i) \cap (\Omega_j \setminus \partial\Omega_j) = \emptyset$, for all $i, j = 1, \ldots, N_{\Omega}$. Conformity implies that, for any two adjacent patches Ω_i and Ω_j , $i \neq j$, with a nonempty (d-1)-dimensional interface $\Gamma_{ij} := \partial\Omega_i \cap \partial\Omega_j$, the pre-images $\hat{\Gamma}_{i\to j} = f_i^{-1}(\Gamma_{ij})$ and $\hat{\Gamma}_{j\to i} = f_j^{-1}(\Gamma_{ij})$ must correspond to facets of the respective reference domains $\hat{\Omega}_i$ and $\hat{\Omega}_j$. Additionally, the tangent vectors at any point $\mathbf{x} \in \Gamma_{ij}$, computed using the two different parametrizations, must coincide [29].

Figure 2 illustrates an example of three conforming patches on a generic two-dimensional domain. The reference domain $\hat{\Omega}$ is mapped onto the three patches Ω_i , i=1,2,3, where conformity is enforced at their interfaces and on points where multiple subdomains meet. Each interface between the individual patches corresponds to either an edge or a corner in the respective reference domain.

4 Multi-patch isogeometric neural solver

4.1 Neural network-based ansatz in the reference domain

The main building blocks of the suggested neural solver are NN-based ansatz functions capable of approximating solutions within the reference domain of IGA, to be then transformed into solutions on the physical geometry. In the following we assume that, for each subdomain (patch) Ω_i , the solution in the reference domain is represented by NN-based ansatz functions $\hat{u}_{\theta_i}: \hat{\Omega}_i \to \mathbb{R}, i=1,\ldots,N_{\Omega}$. These ansatz functions consist of products and superpositions of NNs and polynomials, defined on the reference domain. To ease the notation, the vector $\boldsymbol{\theta} \in \Theta$ concatenates the trainable parameters of all NNs employed in the approximation, such that $\boldsymbol{\theta} = \{\boldsymbol{\theta}_i\}_{i=1}^{N_{\Omega}}$. Accordingly, the patch-specific NN \hat{u}_{θ_i} contains the trainable parameters that correspond to the *i*-th patch only.

The construction of the ansatz functions $\{\hat{u}_{\theta_i}\}_{i=1}^{N_{\Omega}}$ must satisfy the Dirichlet BCs, while also ensuring differentiability within each subdomain and C^0 -continuity across the interfaces between patches. These conditions are particularly advantageous when addressing discontinuous material properties between patches. Utilizing the previously

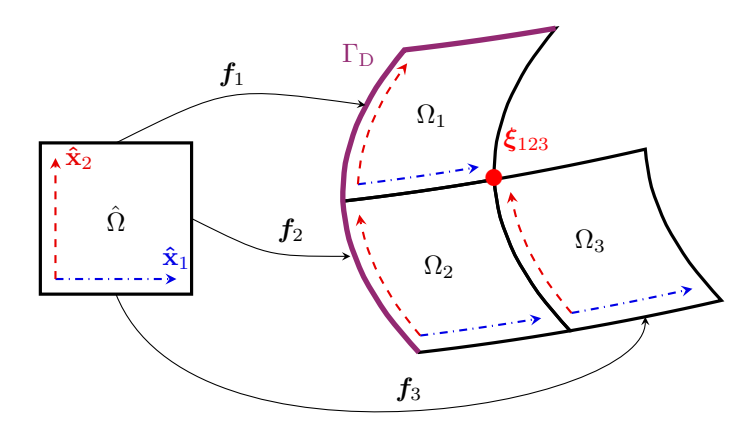


Fig. 2: Example of a two-dimensional domain represented by three patches, Ω_1 , Ω_2 , Ω_3 . The reference domain $\hat{\Omega}$ and the mapping of the reference coordinate system onto each patch are also shown (red and blue dotted lines). The Dirichlet boundary Γ_D is marked in purple. The point $\boldsymbol{\xi}_{123} \in \Omega$ belongs to all three patches simultaneously.

defined pushforward and pullback operations, continuity requires that

$$\hat{u}_{\boldsymbol{\theta}_i} \left(\hat{\Gamma}_{i \to j} \right) = \hat{u}_{\boldsymbol{\theta}_j} \left(\hat{\Gamma}_{j \to i} \right), \tag{10}$$

for every interface Γ_{ij} . Similar to classical approaches found in IGA, condition (10) ensures a continuous transition between individual patches of the multi-patch geometry, by constraining the solution representation in the reference domain. In order to correctly represent situations where boundary elements of different dimensionality intersect, it is necessary to introduce multi-indices. This necessity arises in particular at points where three or more patches of a multi-patch geometry coincide. To guarantee that the continuity condition (10) is satisfied in such configurations, the interface contributions must enforce continuity simultaneously across all interacting patches. To fulfill these requirements, we define our ansatz function within each patch as a superposition of an interior term, $\hat{u}_{\hat{\theta}_i}^{\text{int}}$, representing the solution inside each patch and interface-conforming terms, $\hat{u}_{\hat{\theta}_i}^{j\to i}$, imposing continuity across neighboring patches. The definition reads as follows:

$$\hat{u}_{\boldsymbol{\theta}_{i}}^{(i)} = \hat{u}_{\hat{\boldsymbol{\theta}}_{i}}^{(i,\text{int})} + \sum_{\boldsymbol{j} \in \mathcal{J}(i)} \hat{u}_{\hat{\boldsymbol{\theta}}_{j}}^{\boldsymbol{j} \to i}, \tag{11}$$

where $\mathcal{J}(i)$ is a multi-index set associated with the *i*-the patch, which comprises the multi-indices of all topological entities where the *i*-th patch intersects with other patches, i.e., surfaces (2D), curves (1D), and points (0D), and j are the multi-indices contained therein. For example, considering the two-dimensional domain depicted in

Figure 2, $\mathcal{J}(1) = \{(1,2), (1,2,3)\}$ due to the interface Γ_{12} shared by subdomains Ω_1 and Ω_2 and the point ξ_{123} shared by all three subdomains. Accordingly, $\mathcal{J}(2) = \{(1,2), (2,3), (1,2,3)\}$ and $\mathcal{J}(3) = \{(2,3), (1,2,3)\}$. The interface terms $\hat{u}_{\hat{\theta}_j}^{j \to i}$, $j \in \mathcal{J}(i)$, connect intersecting patches.

The term $\hat{u}_{\hat{\boldsymbol{\theta}}_i}^{(i,\text{int})}$ contributes solely to the interior of the subdomain Ω_i and vanishes on the interfaces defined by the multi-index set $\mathcal{J}(i)$. The trainable parameters per patch are then given as $\boldsymbol{\theta}_i = \hat{\boldsymbol{\theta}}_i \cup \bigcup_{j \in \mathcal{J}(i)} \hat{\boldsymbol{\theta}}_j$. The ansatz functions $\hat{u}_{\boldsymbol{\theta}_i}$ are evaluated separately for the specific patch they correspond to, and collectively yield a global solution. The corresponding ansatz space \mathcal{V}_{Θ} for the physical domain is then defined by the individual parameter spaces Θ of the NNs and the patch-wise inverse pullback:

$$\mathcal{V}_{\Theta} := \left\{ \hat{u}_{\boldsymbol{\theta}_i} \circ \boldsymbol{f}_i^{-1} : i = 1, ..., N_{\Omega} \right\}. \tag{12}$$

The parameter space Θ corresponds to the Cartesian product of the patch-specific parameter spaces which include the parameters of the NNs $\hat{u}_{\theta_i}^{(i)}$, $i=1,\ldots,N_{\Omega}$. The global ansatz function (in the physical domain) is denoted as $u_{\theta} \in \mathcal{V}_{\Theta}$. Note that, for vector-valued ansatz functions $\hat{u}: \hat{\Omega} \to \mathbb{R}^n$, the considerations outlined above can be applied independently to each component (see section 5.2).

4.1.1 Ansatz inside the domains

We first focus on constructing the ansatz within the domain. We assume that the Dirichlet boundary, $\Gamma_{\rm D}$, is derived by applying the pushforward map onto the respective facets of the reference domains. Further, we assume that the Dirichlet data is defined by a function $g_{\rm D}:\Gamma_{\rm D}\to\mathbb{R}^d$ on the Dirichlet boundary. The ansatz is composed of the product of the output of the NN used to approximate the solution in the reference domain, and a polynomial that ensures the enforcement of Dirichlet boundary conditions. The value of the ansatz on the Dirichlet boundary is imposed by adding an additional term to the ansatz. Specifically, the ansatz inside the domain is defined as

$$\hat{u}_{\hat{\boldsymbol{\theta}}_{i}}^{(i,\text{int})}(\hat{\mathbf{x}}) = \mathcal{N}_{\hat{\boldsymbol{\theta}}_{i}}(\hat{\mathbf{x}})\,\hat{p}(\hat{\mathbf{x}}) + (g_{D}\circ\boldsymbol{f})(\hat{\mathbf{x}})\hat{p}_{D}(\hat{\mathbf{x}}),\tag{13}$$

where $\mathcal{N}_{\hat{\boldsymbol{\theta}}_i} : [-1,1]^d \to \mathbb{R}$ is an NN depending on the trainable parameters $\hat{\boldsymbol{\theta}}_i$ and the polynomial $\hat{p}(\hat{\mathbf{x}}) = \prod_{k=1}^d (\hat{x}_k - 1)^{\alpha_k} (\hat{x}_k + 1)^{\beta_k}$ is chosen so that its pullback vanishes on interfaces and Dirichlet boundaries i.e.

$$\hat{p} \circ \mathbf{f}_i^{-1} = 0 \quad \text{for} \quad \mathbf{x} \in \partial \Omega_i \cap \left(\Gamma_{\mathcal{D}} \cup \bigcup_{i \neq j} \partial \Omega_j \right).$$
 (14)

This construction ensures that the product of $\mathcal{N}_{\hat{\theta}_i}$ and \hat{p} yields a parametric function which does not influence Dirichlet boundaries and patch interfaces, however, is variable inside the patch interiors. The inclusion of interfaces in (14) is intentional, as the interface is handled separately by an additional term introduced in the next section.

Using similar principles, we construct the term representing the Dirichlet boundary condition. The choice of the polynomial $\hat{p}_{\rm D}$ must ensure that

$$\hat{p}_{D} \circ \boldsymbol{f}_{i}^{-1} = 1 \text{ for } \mathbf{x} \in \Gamma_{D},$$

$$\hat{p}_{D} \circ \boldsymbol{f}_{i}^{-1} = 0 \text{ for } \mathbf{x} \in \Gamma_{D}^{\text{opp}},$$
(15)

where $\Gamma_{\rm D}^{\rm opp}$ denotes the interface opposing $\Gamma_{\rm D}$. From an implementation point of view, this approach can be interpreted as a custom output layer with a residual connection.

As an example, we revisit the 2D domain composed by 3 patches shown in Figure 2. In the same figure, the mapping of the reference coordinate system onto the physical subdomains is also shown. For simplicity, we assume homogeneous Dirichlet boundary conditions i.e. $g_D = 0$ on Γ_D , where Γ_D is represented by the green line. In the reference domain of Ω_2 , this translates to $\hat{x}_1 = -1$, while for Ω_2 it maps to $\hat{x}_2 = 1$ and $\hat{x}_1 = -1$. There are two interfaces, Γ_{12} and Γ_{13} , and all three domains share a common point ξ_{123} for the multi-index j = (1, 2, 3). Then, the boundary-conforming ansatz inside the domains are:

$$\hat{u}_{\hat{\theta}_{1}}^{(1,\text{int})}(\hat{\mathbf{x}}) = \mathcal{N}_{\hat{\theta}_{1}}(\hat{\mathbf{x}})(\hat{x}_{1}+1)(\hat{x}_{2}+1)(\hat{x}_{2}-1),$$

$$\hat{u}_{\hat{\theta}_{2}}^{(2,\text{int})}(\hat{\mathbf{x}}) = \mathcal{N}_{\hat{\theta}_{2}}(\hat{\mathbf{x}})(\hat{x}_{1}+1)(\hat{x}_{1}-1)(\hat{x}_{2}-1),$$

$$\hat{u}_{\hat{\theta}_{3}}^{(3,\text{int})}(\hat{\mathbf{x}}) = \mathcal{N}_{\hat{\theta}_{3}}(\hat{\mathbf{x}})(\hat{x}_{1}+1)(\hat{x}_{2}+1)(\hat{x}_{2}-1).$$
(16)

4.1.2 Ansatz on domain interfaces

To connect the solutions defined on individual patches, we construct interface-conforming terms. This process is iterative and can be applied to an arbitrary number of dimensions.

We first consider the 0-dimensional intersections that do not belong to the Dirichlet boundary:

$$\Xi_0 = \Big\{ \partial \Omega_i \cap \partial \Omega_j \ : \ \partial \Omega_i \cap \partial \Omega_j \ \text{is 0-dimensional and} \ \partial \Omega_i \cap \partial \Omega_j \not\subseteq \Gamma_{\mathcal{D}} \Big\}. \tag{17}$$

Note that the indices from the set Ξ_0 may have different sizes. Since an element of Ξ_0 may be shared by multiple patches, its pre-image corresponds to different points in the respective reference domains. Given a point $\boldsymbol{\xi} \in \Xi_0$, let $\boldsymbol{j} = \mathcal{I}(\boldsymbol{\xi})$ contain the indices of all patches sharing the 0-dimensional interface $\boldsymbol{\xi}$. Then, the ansatz in all the patches $i \in \boldsymbol{j}$ is expressed as

$$\hat{u}_{\hat{\theta}_{j}}^{j \to i}(\hat{\mathbf{x}}) = \hat{\boldsymbol{\theta}}_{j} \prod_{k=1}^{d} \left((\hat{x}_{k} - 1)^{\alpha_{k}} (\hat{x}_{k} + 1)^{\beta_{k}} \right), \tag{18}$$

where the exponents α_k and β_k are chosen so that the function vanishes at all vertices of the reference domain but $f_i^{-1}(\xi)$. In this case, a single trainable parameters $\hat{\theta}_j$ are responsible for the value of the ansatz on ξ .

Next, we construct the q-dimensional interface ansatz based on the sets Ξ_{q-1}, \ldots, Ξ_0 . The set Ξ_q contains all the q-dimensional interfaces:

$$\Xi_q = \left\{ \partial \Omega_i \cap \partial \Omega_j : \partial \Omega_i \cap \partial \Omega_j \text{ is } q\text{-dimensional and } \partial \Omega_i \cap \partial \Omega_j \not\subseteq \Gamma_D \right\}. \tag{19}$$

Similarly to the 0-dimensional case, for an element $\boldsymbol{\xi} \in \Xi_q$ shared by patches indexed by $\boldsymbol{j} = \mathcal{I}(\boldsymbol{\xi})$, the corresponding ansatz in the *i*-th patch, $i \in \boldsymbol{j} = \mathcal{I}(\boldsymbol{\xi})$, is defined by

$$\hat{u}_{\hat{\theta}_{j}}^{j \to i}(\hat{\mathbf{x}}) = \mathcal{N}_{\hat{\theta}_{j}}(\hat{x}_{l_{1}}, \dots, \hat{x}_{l_{q}}) \prod_{k=1}^{d} ((\hat{x}_{k} - 1)^{\alpha_{k}} (\hat{x}_{k} + 1)^{\beta_{k}}), \tag{20}$$

where the NN $\mathcal{N}_{\hat{\theta}_j}$ is defined on the pre-image $f_i^{-1}(\xi)$, and the coefficients α_k and β_k are chosen such that $\hat{u}_{\hat{\theta}_j}^{j\to i}(\hat{\mathbf{x}}) \circ f_i^{-1}$ vanishes on all q-dimensional faces of the reference domain that do not contain ξ , as well as on all elements of $\Xi_{q-1} \cup \cdots \cup \Xi_0$. This latter condition ensures that the contribution from the q-dimensional interface does not overlap with those from lower-dimensional interfaces. The procedure is iteratively repeated until the set Ξ_{d-1} and the corresponding ansatz functions are constructed.

As an example, we revisit the domain presented in Figure 2. In this case, the set $\Xi_0 = \{\xi_{123}\}$ contains a single element and its corresponding index set is $\mathcal{I}(\xi_{123}) = (1,2,3)$. Then, the interface ansatz functions are

$$\hat{u}^{(1,2,3)\to 1} = \hat{\boldsymbol{\theta}}_{(1,2,3)}(\hat{x}_1 + 1)(\hat{x}_2 - 1),
\hat{u}^{(1,2,3)\to 2} = \hat{\boldsymbol{\theta}}_{(1,2,3)}(\hat{x}_1 + 1)(\hat{x}_2 + 1),
\hat{u}^{(1,2,3)\to 3} = \hat{\boldsymbol{\theta}}_{(1,2,3)}(\hat{x}_1 - 1)(\hat{x}_2 + 1),$$
(21)

where $\hat{\boldsymbol{\theta}}_{(1,2,3)}$ are the trainable parameters corresponding to the common point $\boldsymbol{\xi}_{123}$. The set Ξ_1 contains the two interfaces Γ_{12} and Γ_{23} , with $\mathcal{I}(\Gamma_{12})=(1,2), \mathcal{I}(\Gamma_{23})=(2,3)$. The corresponding interface functions are

$$\hat{u}_{\hat{\boldsymbol{\theta}}_{(1,2)}}^{(1,2)\to 1} = \mathcal{N}_{\hat{\boldsymbol{\theta}}_{(1,2)}}(\hat{x}_1)(\hat{x}_1+1)(\hat{x}_1-1)(\hat{x}_2-1),$$

$$\hat{u}_{\hat{\boldsymbol{\theta}}_{(1,2)}}^{(1,2)\to 2} = \mathcal{N}_{\hat{\boldsymbol{\theta}}_{(1,2)}}(\hat{x}_1)(\hat{x}_1+1)(\hat{x}_1-1)(\hat{x}_2+1),$$

$$\hat{u}_{\hat{\boldsymbol{\theta}}_{(2,3)}}^{(2,3)\to 2} = \mathcal{N}_{\hat{\boldsymbol{\theta}}_{(2,3)}}(\hat{x}_2)(\hat{x}_1+1)(\hat{x}_2+1)(\hat{x}_2-1),$$

$$\hat{u}_{\hat{\boldsymbol{\theta}}_{(2,3)}}^{(2,3)\to 3} = \mathcal{N}_{\hat{\boldsymbol{\theta}}_{(2,3)}}(\hat{x}_2)(\hat{x}_1-1)(\hat{x}_2+1)(\hat{x}_2-1).$$
(22)

In this case, the NNs used are restricted to only one of the coordinates. Moreover, the Dirichlet boundary as well as the set Ξ_0 are taken into account for the interfaces corresponding to Γ_{12} .

To illustrate how the ansatz functions are constructed on domain interfaces, we refer to Figure 3. On the left-hand side, the interface functions from equation (21) spanning three subdomains are omitted, but the planes where continuity must be

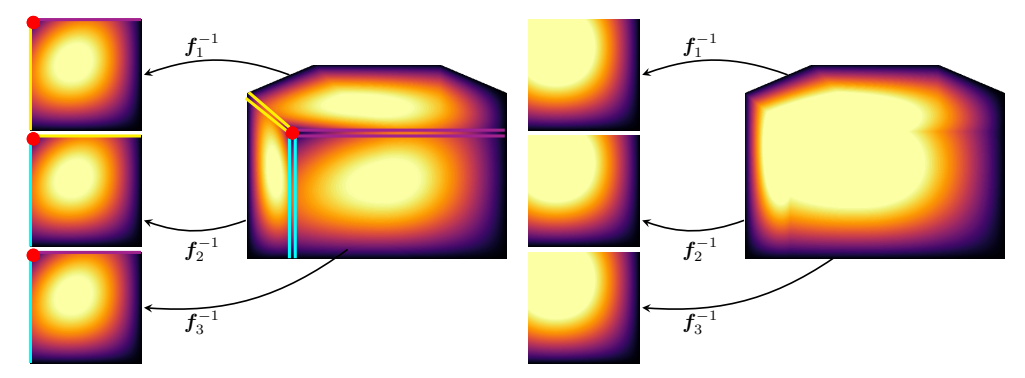


Fig. 3: Illustration of the construction of interface ansatz functions. At the point where multiple subdomains meet, indicated by the red circle, the interface functions take zero values. Continuity is enforced at the interfaces indicated by the colored lines (yellow, cyan, and purple) in the reference and physical domains.

enforced in both the parametric and physical domains are indicated. The red circle marks the coincidence point of all three subdomains (similar to point ξ_{123} in Figure 1). On the right-hand side, the complete ansatz function is shown, incorporating all interface functions. As can be observed, continuity is enforced across all patches.

5 Numerical examples

In this section, the suggested neural solver is used for, first, a 2D magnetostatics simulation, and, second, a 3D solid mechanics simulation involving nonlinear material behavior and nonlinear BCs. In both examples, we begin with the formulation of the problem at hand and then proceed with implementation details and the corresponding numerical results.

5.1 Magnetostatic simulation of a quadrupole magnet

5.1.1 Magnetostatic formulation

We consider the magnetostatic problem setting, which can be retrieved by considering the eddy-current problem and dropping the time dependencies and conductive materials [65]. Under these assumptions, the problem can be formulated in terms of the magnetic vector potential. If the problem is reduced to 2D, only the longitudinal component $u: \Omega \to \mathbb{R}$ of the magnetic vector potential is required [65]. In this case, the governing equation for a linear isotropic material is

$$-\mathbf{grad} (\nu \, \mathbf{grad} u) = j_z, \quad \text{in } \Omega,$$

$$u = 0, \quad \text{on } \Gamma_{D},$$

$$\nu \, \mathbf{grad} u \cdot \boldsymbol{n} = 0, \quad \text{on } \Gamma_{N},$$
(23)

where Ω is the computational domain, j_z is the z-component of the excitation current density, $\Gamma_{\rm D}$ the Dirichlet boundary and $\Gamma_{\rm N}$ the Neumann boundary. An energy functional minimization problem of the form (3) can be derived, where the energy functional is given as

$$I(u) = \frac{1}{2} \int_{\Omega} \nu \operatorname{\mathbf{grad}} u \cdot \operatorname{\mathbf{grad}} u \, d\mathbf{x} - \int_{\Omega} u j_z \, d\mathbf{x}. \tag{24}$$

By taking into consideration a multi-patch decomposition of the domain Ω as shown in section 3.3, the evaluation of the energy functional in the reference domain yields

$$I(\hat{u}_{\theta}) = \frac{1}{2} \sum_{i=1}^{N_{\Omega}} \int_{\hat{\Omega}_{i}} \nu \operatorname{\mathbf{grad}}(\hat{u}_{\theta})^{\mathsf{T}} \mathbf{K}^{(i)}(\hat{\mathbf{x}}) \operatorname{\mathbf{grad}}(\hat{u}_{\theta}) d\hat{\mathbf{x}} - \int_{\hat{\Omega}_{s}} j_{z} \cdot \hat{u}_{\theta} |\det D\mathbf{f}_{i}| d\hat{\mathbf{x}},$$
(25)

where $\mathbf{K}^{(i)}(\hat{\mathbf{x}}) = (D\mathbf{f}_i)^{-\intercal}(D\mathbf{f}_i)^{-1} |\det D\mathbf{f}_i|$ and $\hat{\Omega}_s$ is the reference domain corresponding to the patch that contains the source current excitation. The ansatz function \hat{u}_{θ} is constructed to naturally enforce homogeneous Dirichlet boundary conditions, hence, we do not require additional penalization terms.

For the material distribution, we consider linear magnetic materials, where $\mu_0 = 4\pi \cdot 10^{-7} \frac{\text{H}}{\text{m}}$ is the permeability of free space, $\mu_{\text{Fe}} = 2000 \mu_0$ the permeability of iron, and $\mu_{\text{Cu}} \approx \mu_0$ the permeability of copper. For the excitation, we consider a constant current density $j_z = 7.95 \cdot 10^8 \frac{\text{A}}{\text{m}^2}$.

To quantify error, we use the relative L^2 error, given by the formula

$$\epsilon_{\text{rel},L^2(\Omega)} = \frac{\left\| u_{\boldsymbol{\theta}} - u^{\text{FEM}} \right\|_{L^2(\Omega)}}{\left\| u^{\text{FEM}} \right\|_{L^2(\Omega)}},\tag{26}$$

where u^{FEM} is a highly resolved FEM solution. For both computational examples, we calculate the relative L^2 error, once on the complete domain Ω and for the individual subdomains $\Omega_1, ..., \Omega_{N_{\Omega}}$. This approach enables us to assess the overall error across the domain and analyze its distribution.

5.1.2 Simple quadrupole magnet model

First, we consider a relatively simple quadrupole magnet geometry, depicted in Figure 4. On the left hand side of Figure 4, the complete cross-section of the quadrupole magnet is depicted. On the right hand side of Figure 4, one eighth of the magnet's geometry is shown, exploiting its rotational symmetry. The latter constitutes the domain geometry of the computational model and is partitioned into patches $\Omega_1, \ldots, \Omega_4$. The characterization "simple" is due to the fact that only four patches are required for the complete parametrization of Ω . The purple shading highlights the location of the computational model's domain on the complete cross-section domain. The iron yoke is shown in gray, the current excitations in yellow, and the air domain in white. Dirichlet and Neumann boundary conditions are applied at the boundaries as indicated.

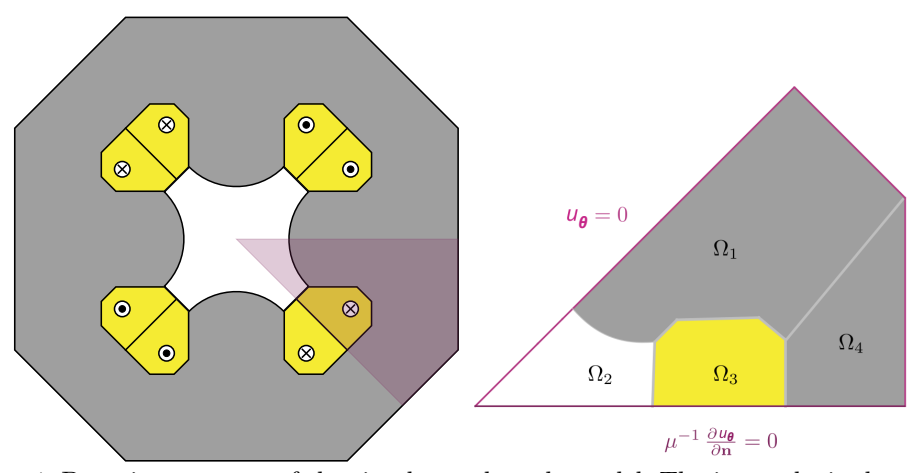


Fig. 4: Domain geometry of the simple quadrupole model. The iron yoke is shown in gray, the current excitations in yellow, and the air gap in white. The purple shading indicates the model section in the symmetry planes. **Left:** Full cross-section. **Right:** One-eighth of cross-section, exploiting rotational symmetry. The domain is partitioned into patches Ω_i , $i = 1, \ldots, 4$.

A residual neural network (ResNet) architecture [66] is chosen for the NNs on both the subdomains and on the interfaces. In particular, we employ NNs with four fully connected (FC) layers, including an input layer, one ResNet block, and an output layer. The number of neurons in each layer varies depending on whether the NN is allocated to the domain or to an interface. That is, more neurons are allocated for the domain compared to the interface. For the domain-NNs, we employ 16 neurons per layer, and the input and output dimensions for each FC layer vary throughout the network according to $(2,16) \rightarrow (16,16) \rightarrow (16,16) \rightarrow (16,1)$. For the interface-NNs, we employ eight neurons per layer, and the input and output dimensions for each FC layer vary according to $(1,8) \to (8,8) \to (8,8) \to (8,1)$. In both cases, there exist two skip connections, before the second and fourth layer, respectively. The hyperbolic tangent activation function is used. The NNs are trained for 1000 epochs, utilizing 4×10^4 Monte Carlo sampling points in each epoch. For the reference solution, we employ the FEniCS FEM solver [67, 68], using a first-order tetrahedral mesh consisting of 13957 elements. Table 1 provides an overview of the NN and trainable parameters employed in this use-case.

Table 1: Distribution of NNs and trainable parameters for the simple quadrupole model.

| | Number of NNs | Number of trainable parameters |
|-----------------------|---------------|--------------------------------|
| Point interfaces (0D) | - | 2 |
| Interface NNs (1D) | 5 | 108 |
| Domain NNs (2D) | 4 | 360 |
| Total | 9 | 1982 |

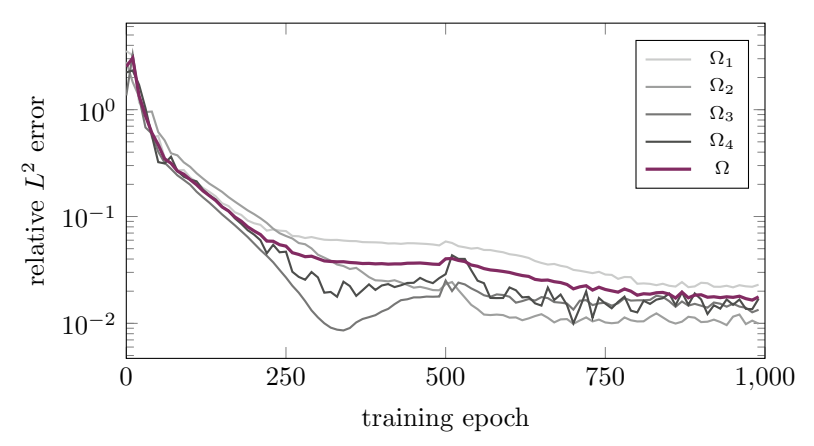


Fig. 5: Relative L^2 error during training for the entire computational domain and for each subdomain and the simple quadrupole model.

A plot of the relative L^2 error over the entire training process is displayed in Figure 5, concerning the full computational domain Ω and the individual patches $\Omega_1, \ldots, \Omega_4$. Even though a low absolute error is obtained throughout the domain, the maximal error occurs in the subdomain Ω_1 , in particular in areas where the NURBS parametrization exhibits non-smooth behavior. This is also observed in Figure 6, which shows the absolute error over the computational domain. The minimum relative L^2 error over Ω is $1.77 \cdot 10^{-2}$.

5.1.3 Complex quadrupole magnet model

Next, we consider a more complex quadrupole magnet geometry, depicted in Figure 7. The left hand side of Figure 7 shows the complete cross-section of the quadrupole magnet, while the right hand side shows one eighth of its geometry, exploiting its rotational symmetry. The latter constitutes the domain geometry of the computational model and is partitioned into patches $\Omega_1, ..., \Omega_9$. The material distribution and coloring scheme is identical to Figure 4. There are 5 more NURBS parametrizations than in the previous section, hence the characterization "complex". The ansatz function for this example is more intricate, as conformity must be ensured over nine patches instead of four. Again, Dirichlet and Neumann boundary conditions are applied at the boundaries as indicated.

Again, a ResNet architecture is employed for both the domain- and interface-NNs. In this case, we employ NNs with five FC layers, including an input layer, one ResNet block, and an output layer. For the domain-NNs, we employ two variations of the same architecture. In subdomains Ω_1 and Ω_2 , we allocate 16 neurons per layer, such that the input and output dimensions for each FC layer vary throughout the network according to $(2,16) \rightarrow (16,16) \rightarrow (16,16) \rightarrow (16,16) \rightarrow (16,1)$. For the rest subdomains, we allocate eight neurons per layer, such that the input and output dimensions vary according to $(2,8) \rightarrow (8,8) \rightarrow (8,8) \rightarrow (8,8) \rightarrow (8,1)$. For the interface-NNs, we employ five neurons per layer and the input and output dimensions for each FC layer

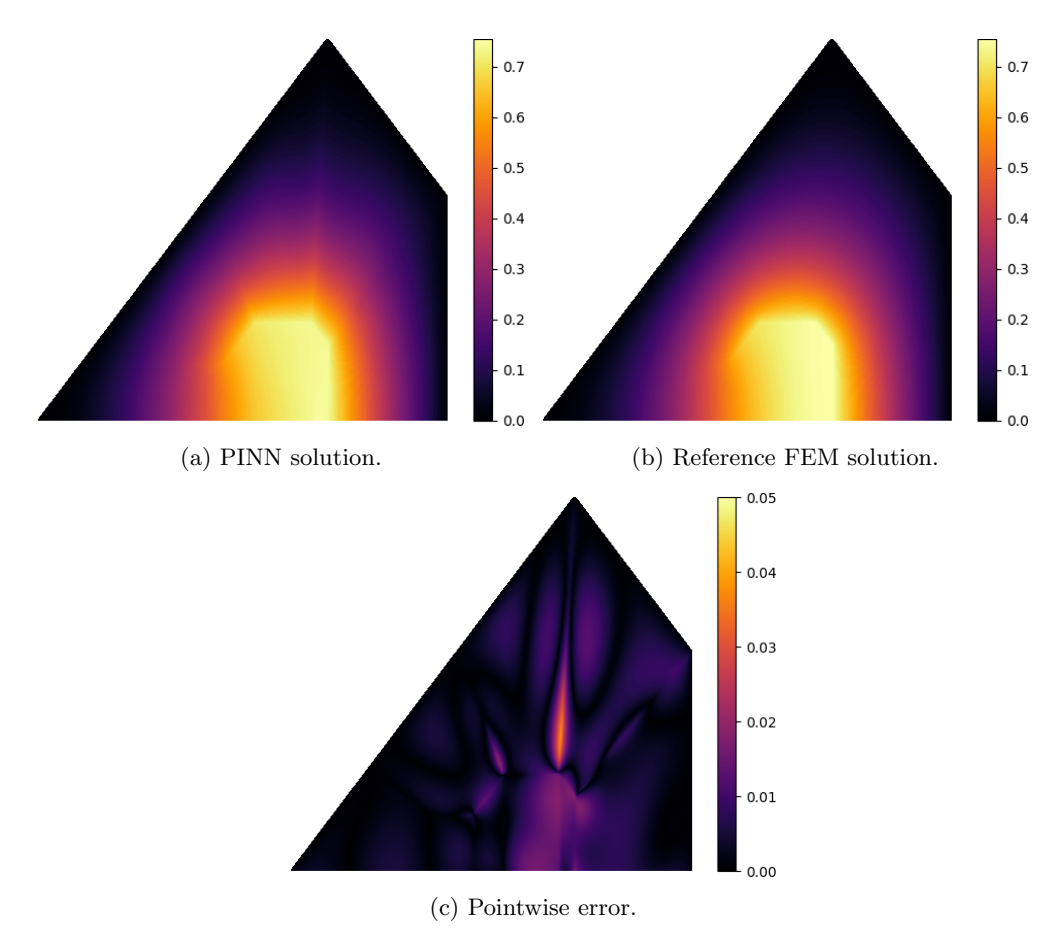


Fig. 6: Field solutions and corresponding error field for the simple quadrupole magnet model.

vary according to $(1,5) \to (5,5) \to (5,5) \to (5,5) \to (5,1)$. In both cases there are two skip connections, before the third and the final layer, respectively. The activation function used is the hyperbolic tangent function $\sigma(x) = \tanh(x)$. The NNs are trained for 1000 epochs, utilizing 1.8×10^5 Monte Carlo sampling points per epoch. For the reference solution, we employ the FEniCS FEM solver [67, 68], using a first-order tetrahedral mesh consisting of 770743 elements. Table 2 we provides an overview of the NN and trainable parameters employed in this use-case.

Similar to the previous section, the NNs are trained for 1000 training epochs and the relative L^2 error is calculated with respect to an FEM reference solution using $4\cdot10^4$ quadrature points. The relative L^2 error over the entire training process is displayed in Figure 8 for both the full computational domain and its subdomains. Although the absolute error is consistently low across the domain, the highest error occurs within the subdomain Ω_2 , particularly in areas where the NURBS parameterization displays

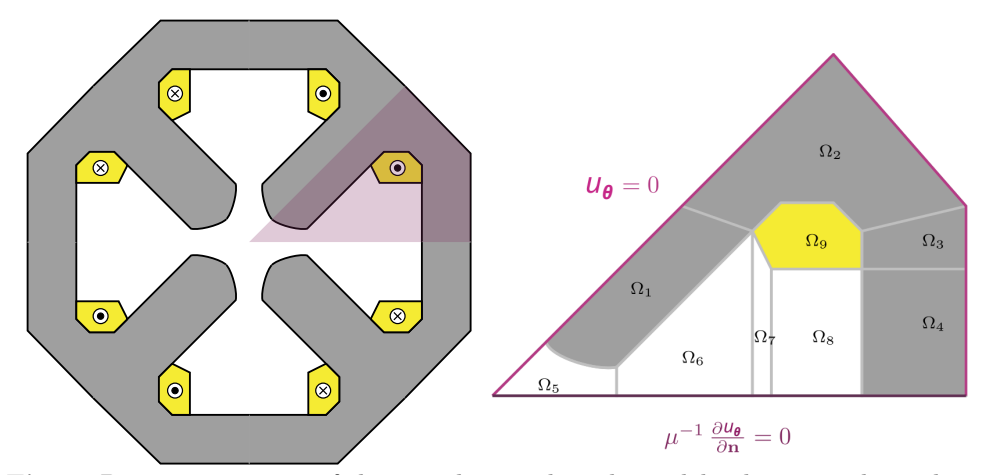


Fig. 7: Domain geometry of the complex quadrupole model. The iron yoke is shown in gray, the current excitations in yellow, and the air gap in white. The purple shading indicates the model section in the symmetry planes. **Left:** Full cross-section. **Right:** One-eighth of cross-section, exploiting rotational symmetry. The domain is partitioned into patches Ω_i , $i = 1, \ldots, 9$.

non-smooth behavior. This is also evident in Figure 9c, which shows of the absolute pointwise error over the quadrupole's computational domain. The minimum relative L^2 error over Ω is $6.05 \cdot 10^{-3}$.

5.2 Solid mechanics simulation of mechanical holder

5.2.1 Solid mechanics formulation

We now consider a problem in the setting of nonlinear solid mechanics. Given a domain $\Omega \subset \mathbb{R}^d$, d=2,3, composed of N_{Ω} patches, we define the displacement field $\boldsymbol{u}:\Omega \to \mathbb{R}^d$, which describes the deformation of the domain Ω . Then, given a point $\mathbf{x} \in \Omega$, its position in the deformed configuration is given by $\varphi(\mathbf{x}) = \mathbf{x} + \boldsymbol{u}(\mathbf{x})$. The task is to

Table 2: Distribution of NNs and trainable parameters for the complex quadrupole model.

| | Number of NNs | Number of trainable parameters |
|---|---------------|--------------------------------|
| Point interfaces (0D) | - | 5 |
| Interface NNs (1D) | 13 | 74 |
| Domain NNs for $\Omega_3 - \Omega_9$ (2D) | 7 | 183 |
| Domain NNs for Ω_1 , Ω_2 (2D) | 2 | 615 |
| Total | 22 | 3478 |

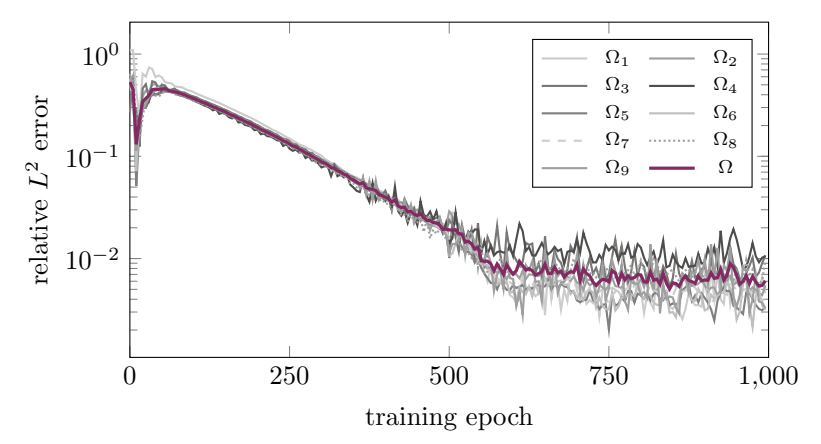


Fig. 8: Relative L^2 error during training for the entire computational domain and for each subdomain and the complex quadrupole model.

find the displacement that minimizes the total potential energy [69]:

$$\min_{\boldsymbol{u} \in \mathcal{V}} I(\boldsymbol{u}) = \min_{\boldsymbol{u}} \sum_{i=1}^{N_{\Omega}} \left(\int_{\Omega_{i}} \psi(\boldsymbol{u}) \, d\mathbf{x} - \int_{\Omega_{i}} \boldsymbol{b} \cdot \boldsymbol{u} \, d\mathbf{x} - \int_{\Gamma_{i}} \boldsymbol{T} \cdot \boldsymbol{u} \, d\sigma(\mathbf{x}) \right), \quad (27)$$

where \mathcal{V} is a suitable space of all possible displacements satisfying the boundary conditions, ψ is the stored energy density, \boldsymbol{b} is the body force, and \boldsymbol{T} is the surface traction prescribed on some parts of the boundary $\Gamma_i \subset \partial\Omega, i=1,...,N_{\Omega}$. The boundaries are considered to be the union of images of facets in the reference domain, such that $\Gamma_i = \boldsymbol{f}_i(\hat{\Gamma}_i)$. Both body forces and surface traction are defined in the undeformed configuration. In this work we use the Saint Venant–Kirchhoff material model [69] with the stored energy density

$$\psi = \frac{\lambda}{2} (\operatorname{tr} \mathbf{E})^2 + \mu \mathbf{E} \cdot \mathbf{E}, \tag{28}$$

where $E = \frac{1}{2}(FF^{\top} - I)$ is the Green strain tensor, $F = I + \mathbf{grad}u$ is the deformation gradient and λ , μ are the Lamé coefficients. The formulation can be expressed in the reference domains $\hat{\Omega}_i$ as

$$I(\hat{\boldsymbol{u}}) = \sum_{i=1}^{N_{\Omega}} \left(\int_{\hat{\Omega}_{i}} \hat{\psi}(\hat{\boldsymbol{u}}) |\det D\boldsymbol{f}_{i}| \, d\hat{\mathbf{x}} - \int_{\Omega_{i}} \boldsymbol{b} \cdot \hat{\boldsymbol{u}} \, |\det D\boldsymbol{f}_{i}| \, d\hat{\mathbf{x}} - \int_{\Gamma_{i}} \boldsymbol{T} \cdot \boldsymbol{u} ||D\boldsymbol{f}_{i}\boldsymbol{\nu}|||\det D\boldsymbol{f}_{i}| \, d\sigma(\hat{\mathbf{x}}) \right),$$
(29)

where $\hat{\psi} = \frac{\lambda}{2} (\operatorname{tr} \hat{\boldsymbol{E}})^2 + \mu \hat{\boldsymbol{E}} \cdot \hat{\boldsymbol{E}}, \ \hat{\boldsymbol{E}} = \frac{1}{2} (\hat{\boldsymbol{F}} \hat{\boldsymbol{F}}^{\top} - \boldsymbol{I})$ and $\hat{\boldsymbol{F}} = \boldsymbol{I} + (\operatorname{\mathbf{grad}} \hat{\boldsymbol{u}}) (D\boldsymbol{f}_i)^{-1}$ and $\boldsymbol{\nu}_i, i = 1, ..., N_{\Omega}$ are the unit normals.

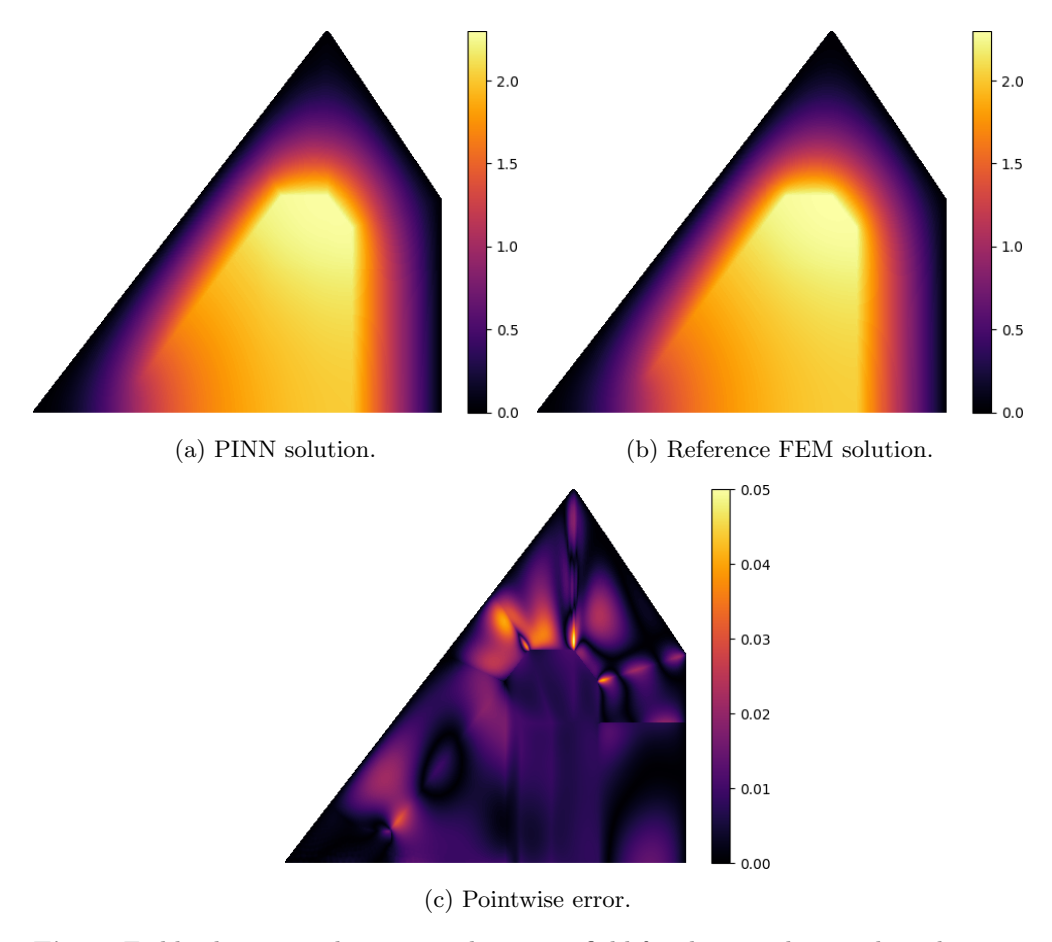


Fig. 9: Field solutions and corresponding error field for the complex quadrupole magnet model.

A further topic of interest in solid mechanics simulations are contact boundary conditions. In this work, we consider a second body, denoted as $\Omega^r \subset \mathbb{R}^d$, which is rigid and not part of the computational domain (see Figure 10). To prevent the penetration of the two bodies, we use the penalty approach [70]. The idea is to apply a traction along the boundary subdomain where the penetration occurs. To that end, we define the penetration distance function from a point $\varphi(\mathbf{x}), \mathbf{x} \in \partial \Omega$ to the body Ω^r as

$$g_{\Omega^{\mathrm{r}}}(\boldsymbol{\varphi}, \mathbf{x}) = \begin{cases} \min_{\boldsymbol{x}' \in \Omega^{\mathrm{r}}} ||\boldsymbol{\varphi}(\mathbf{x}) - \mathbf{x}'||_{2}^{2}, & \boldsymbol{\varphi}(\mathbf{x}) \text{ penetrates } \Omega^{\mathrm{r}}, \\ 0, & \text{otherwise.} \end{cases}$$
(30)

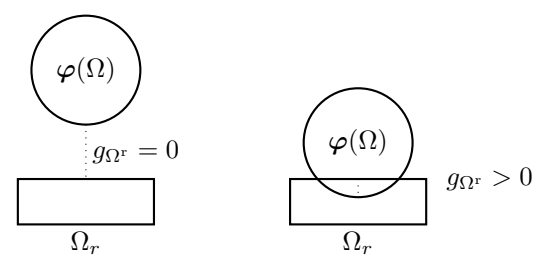


Fig. 10: Illustration of the penetration distance between a rigid body $\Omega^{\rm r}$ and the deformed configuration $\varphi(\Omega)$. On the left, the penetration distance is zero as no penetration yet exists. On the right, the penetration distance becomes strictly positive.

The following penalty is introduced:

$$I_{\rm C} = \frac{1}{2} \int_{\partial\Omega} \epsilon_{\rm N} g_{\Omega^{\rm r}}^2(\boldsymbol{\varphi}, \mathbf{x}) || \boldsymbol{F}^{-\top} \boldsymbol{N} ||_2 \det \boldsymbol{F} \, d\sigma(\mathbf{x}), \tag{31}$$

where N is the normal vector on the undeformed boundary and $\epsilon_{\rm N} > 0$ is a penalty constant. The integral can be expressed in the reference configuration using (29). By adding the penalty and the potential energy and introducing the conformal ansatz functions, denoted by u_{θ} , the final optimization problem to be solved is:

$$\min_{\boldsymbol{u}_{\boldsymbol{\theta}} \in \mathcal{V}} I(\boldsymbol{u}_{\boldsymbol{\theta}}) + I_{\mathbf{C}}(\boldsymbol{u}_{\boldsymbol{\theta}}). \tag{32}$$

The penalty term expressed in (31) is also nonlinear with respect to the displacement. Conventional FEM based methods employ Newton's method to cope with the nonlinearity. In the case of nonlinear solid mechanics with contact boundary conditions, incremental loading (displacement applied on boundary, body forces or boundary traction) is used to avoid the divergence of the Newton iterations due to badly selected starting points, and the previous increment is used as a starting point for the next. In the framework developed in this work, we solve the stationary problem directly. The load can be added as an additional input to the NNs that approximate the solution.

5.2.2 Mechanical holder model

In this section, we examine a structural holder, the geometry of which is depicted in Figure 11. The computational domain consists of five NURBS patches, also shown in Figure 11. To model the material behavior, we utilize the Saint Venant-Kirchhoff constitutive law presented in (28), with the Lamé parameters $\lambda = \frac{E\nu}{(1+\nu)(1-2\nu)}$ and $\mu = \frac{E}{2(1+\nu)}$, where the Young's modulus is E=2000 MPa and the Poisson's ratio is $\nu=0.3$.

The mechanical setup includes two rigid half-planes, defined by the relations $x_2 = -0.75 - 0.05\phi_1$ for $x_1 \le 1$, and $x_2 = 0.75 + 0.05\phi_2$ for $x_1 \le 1$, which make contact

with the domain. The variables $\phi_1, \phi_2 \in [-1, 1]$ serve as additional inputs to the NNs that control the boundary conditions. The object is fixed at $x_1 = 2.75$ by imposing a zero Dirichlet boundary condition on the displacement.

The solution is approximated using a total of twelve NNs, where five NNs are employed for the five subdomains, five NNs are defined on the surface interfaces between the domains, and two NNs are defined on the line interfaces where three domains meet. All NNs have the same architecture, consisting of a single fully connected input layer, followed by two residual blocks. Each residual block contains two hidden layers with 16 neurons each, thus resulting in a total of 14676 trainable parameters. The layer by layer structure is $(d+2,16) \rightarrow [(16,16) \rightarrow (16,16)] \rightarrow [(16,16) \rightarrow (16,3)]$, where d is the dimensionality of the manifold the network is defined on and 2 stands for the number of parameters. A detailed overview is given in Table 3. The activation function used is the squared ReLU $\sigma(x) = \max(x^2,0)$. The NNs are trained for 64 epochs, utilizing 8×10^6 Monte Carlo sampling points per epoch, divided into 1000 batches. The training process is executed on an Nvidia RTX 4090 laptop GPU, with a total runtime of 13 minutes. For the reference solution, we employ

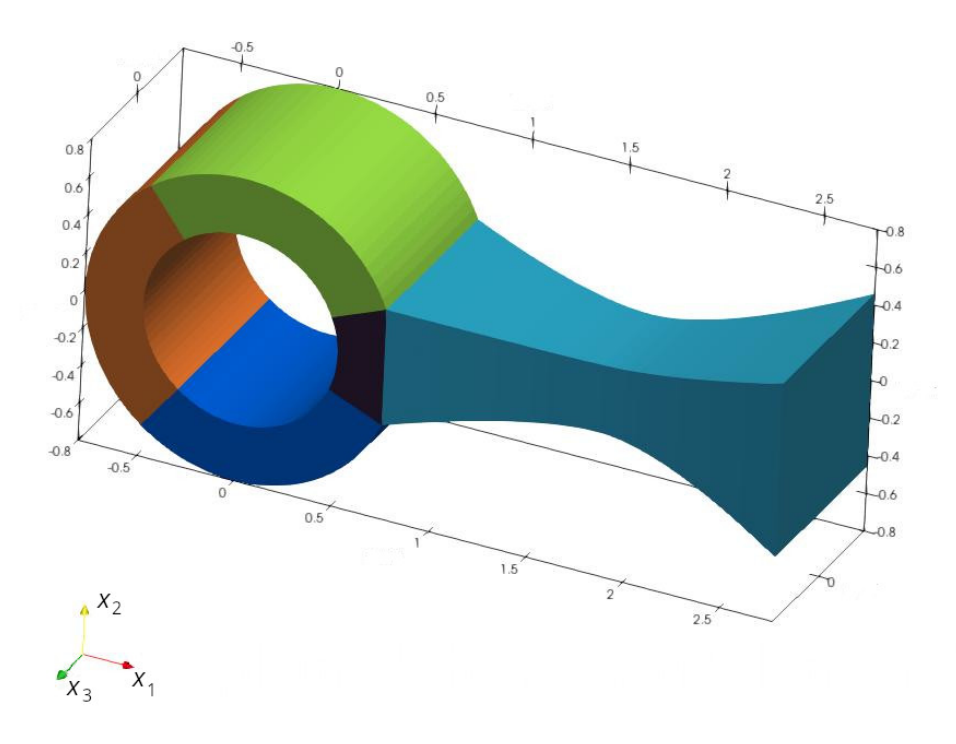


Fig. 11: Geometry of the mechanical holder model, parametrized with five NURBS patches, each shown with a different color. All dimensions are expressed in mm.

the CalculiX finite element solver [71], using a first-order tetrahedral mesh consisting of 770743 elements.

The results are presented in Figures 13-15, where both the deformed configurations and the pointwise error fields are shown for the parameter combinations $(\phi_1, \phi_2) \in \{(-1, -1), (-1, 1), (1, -1)\}$. All shown results correspond to a 2D slice at $x_3 = 0$. The case $(\phi_1, \phi_2) = (1, 1)$ represents a configuration with no contact and where no deformation exists. As a parameter dependent error metric, we use the error metric defined in (26), where \boldsymbol{u} represents the predicted displacement field and $\boldsymbol{u}^{\text{FEM}}$ is the reference solution. The error is evaluated over a Cartesian grid defined on each individual NURBS patch. The number of grid points is N=75000, corresponding to a uniform grid on the reference domain. The error values for the different parameter combinations of ϕ_1 and ϕ_2 are given in Table 4. The behavior of the error during training is shown in Figure 12.

6 Conclusion

This paper presented a novel methodology combining PINNs with the IGA framework tailored for complex, multi-patch domains common in CAD. Our core contribution lies in formulating the PINN approximation within the reference domain of individual IGA patches, ensuring geometric fidelity. Solution continuity across patch interfaces was achieved through the introduction of dedicated interface NNs, while the strong enforcement of Dirichlet boundary conditions was realized via a specific NN output ansatz, drawing parallels to domain decomposition techniques similar to FETI and mortaring methods.

The efficacy and versatility of the developed multi-patch isogeometric neural solver was validated through complex numerical examples related to real-world applications.

Table 3: Distribution of NNs and trainable parameters for the mechanical holder model.

| | Number of NNs | Number of trainable parameters |
|--------------------|---------------|--------------------------------|
| Domain NNs (3D) | 5 | 1235 |
| Interface NNs (2D) | 5 | 1219 |
| Interface NNs (1D) | 2 | 1203 |
| Total | 12 | 14676 |

| ϕ_1 | ϕ_2 | $\epsilon_{\mathrm{rel},L^2}$ |
|----------|----------|-------------------------------|
| -1 | -1 | 0.0136 |
| -1 | 1 | 0.0264 |
| 1 | -1 | 0.0266 |

Table 4: Relative L^2 error for different combinations of ϕ_1 and ϕ_2 .

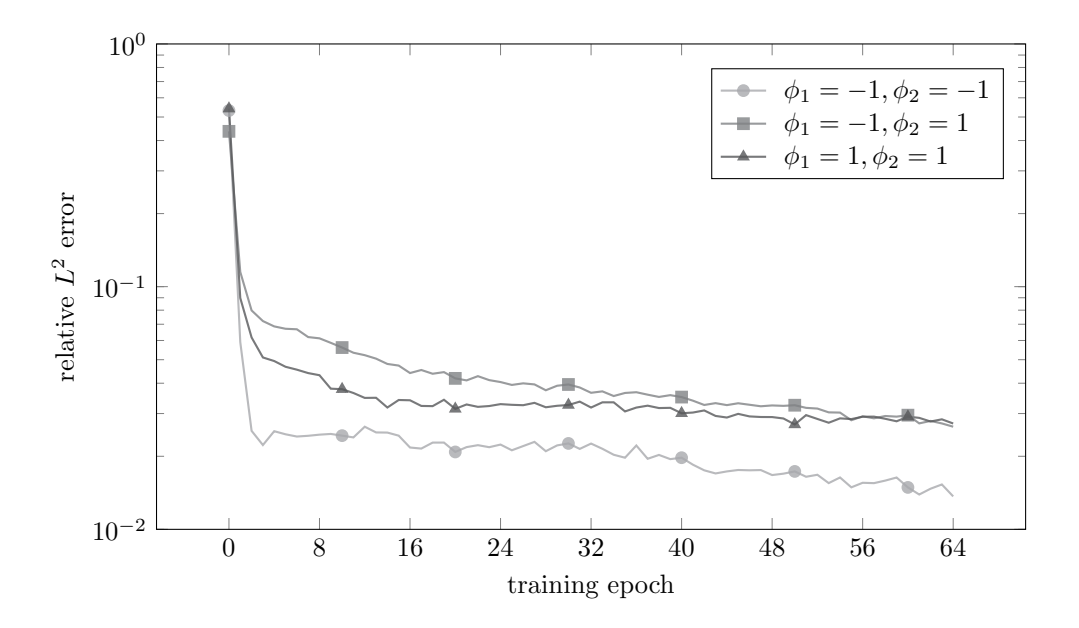
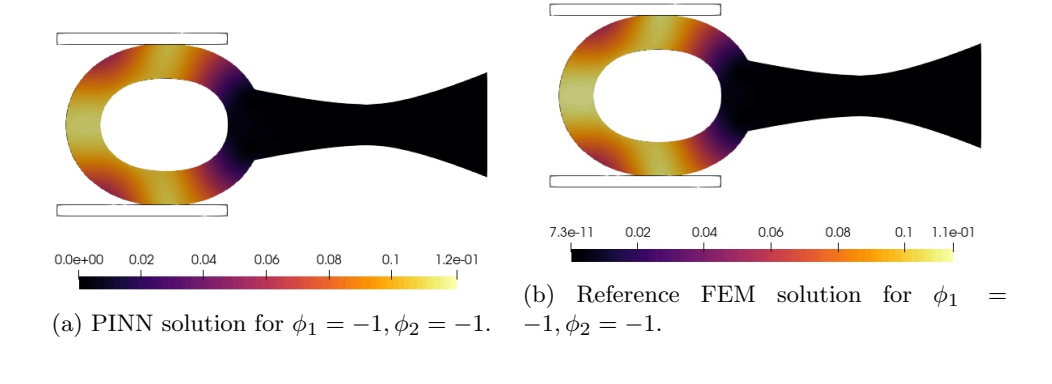


Fig. 12: Relative L^2 error during training for the entire computational domain and for different combinations of the parameters ϕ_1, ϕ_2 .

We successfully applied the framework to both 2D magnetostatic simulations, involving simple and complex quadrupole magnet geometries, and a 3D nonlinear solid mechanics problem featuring hyperelastic material behavior, contact boundary conditions, and parametric dependencies. Quantitative numerical error analyses against reference solutions demonstrated the accuracy and robustness of the proposed method.

This work contributes towards bridging the gap between native CAD representations and mesh-free simulation capabilities offered by PINNs. By effectively handling complex multi-patch geometries and ensuring strong enforcement of essential boundary and interface conditions, our framework overcomes key limitations of standard PINNs and provides a powerful tool for analyzing complex physical systems directly within their design context.

Naturally, the suggested neural solver comes with a set of limitations, which we plan to address in future studies. First, suitable NN architectures are selected empirically and by trial and error. Since the focus of this work is on embedding PINNs into the IGA framework, a systematic study on specific NN architectures remains out of scope, leaving many questions regarding design and optimization open for future research. The neural solver is also not yet competitive to traditional numerical solution methods in terms of computational efficiency, due to the required NN training times. Limitations related to those encountered in conventional IGA also exist. For example, the suggested neural solver requires interface-conforming patches, for which no automatic generation procedure exists, even in conventional IGA. Moreover, the



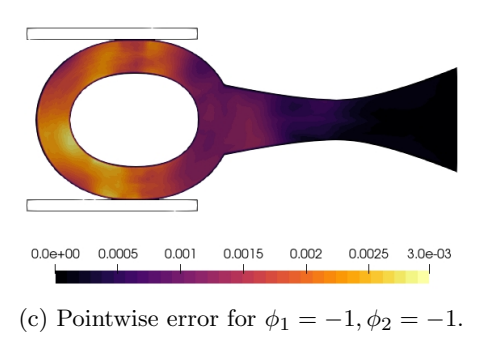
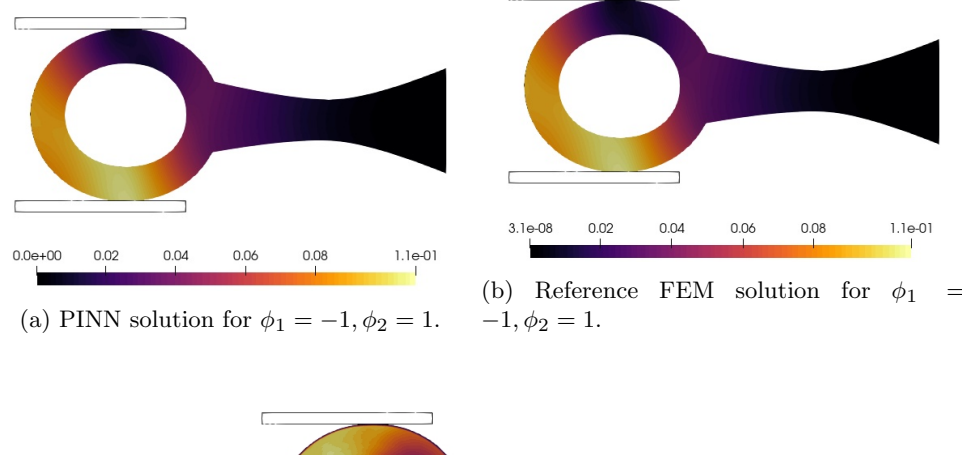


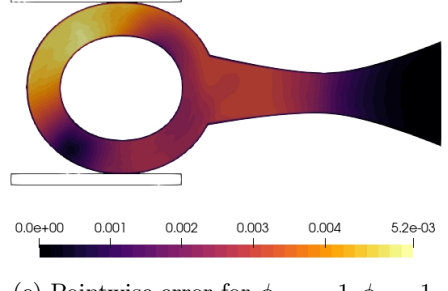
Fig. 13: Field solutions and corresponding error field for the mechanical holder model with contact parameters $\phi_1 = -1$, $\phi_2 = -1$. A 2D slice at $x_3 = 0$ is used for the visualization.

imposition of the Dirichlet boundary condition still lacks the Kronecker delta property, which is a known limitation of IGA compared to classical FEM. Last, the neural solver is currently limited to enforcing C^0 -continuity only. Extensions to higher regularities remain to be addressed.

Last, in addition to resolving the aforementioned limitations, the generalization of the suggested neural solver to parametric problem formulations, in particular high-dimensional ones, constitutes an open and highly relevant future research direction. From the perspective of the authors, research on parametric problems that leverages optimized, problem-specific NN architectures holds significant potential to surpass conventional methods, similar to the successes of NNs in fields such as image classification and natural language processing.

Author contributions. MvT and IGI developed the methodology, implemented the software, and performed all simulations and numerical studies. DL acquired funding and provided supervision. All authors contributed to writing and reviewing the manuscript.



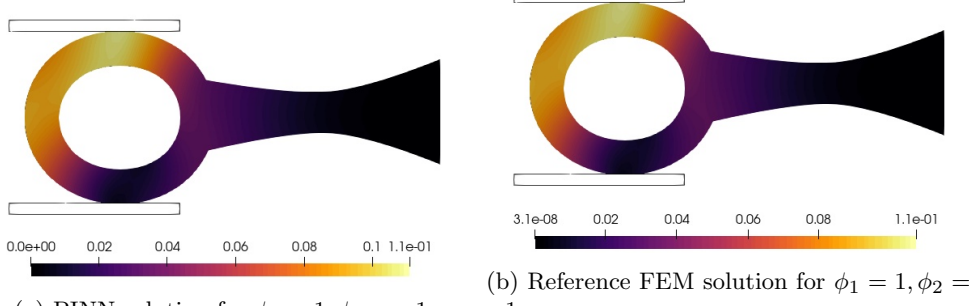


(c) Pointwise error for $\phi_1 = -1, \phi_2 = 1$.

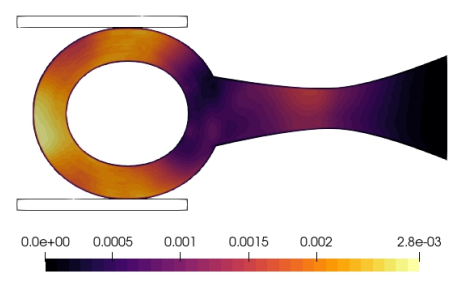
Fig. 14: Field solutions and corresponding error field for the mechanical holder model with contact parameters $\phi_1 = -1$, $\phi_2 = 1$. A 2D slice at $x_3 = 0$ is used for the visualization.

References

- [1] Raissi, M., Perdikaris, P., Karniadakis, G.E.: Physics-informed neural networks: A deep learning framework for solving forward and inverse problems involving nonlinear partial differential equations. Journal of Computational physics 378, 686–707 (2019)
- [2] Anitescu, C., İsmail Ateş, B., Rabczuk, T.: Physics-informed neural networks: Theory and applications. In: Machine Learning in Modeling and Simulation: Methods and Applications, pp. 179–218. Springer, ??? (2023)
- [3] Kim, D., Lee, J.: A review of physics informed neural networks for multiscale analysis and inverse problems. Multiscale Science and Engineering **6**(1), 1–11 (2024)
- [4] E, W., Yu, B.: The deep ritz method: a deep learning-based numerical algorithm



(a) PINN solution for $\phi_1 = 1, \phi_2 = -1$.



(c) Pointwise error for $\phi_1 = 1, \phi_2 = -1$.

Fig. 15: Field solutions and corresponding error field for the mechanical holder model with contact parameters $\phi_1 = 1$, $\phi_2 = -1$. A 2D slice at $x_3 = 0$ is used for the visualization.

for solving variational problems. Communications in Mathematics and Statistics **6**(1), 1–12 (2018)

- [5] Sirignano, J., Spiliopoulos, K.: Dgm: A deep learning algorithm for solving partial differential equations. Journal of computational physics 375, 1339–1364 (2018)
- [6] Yang, L., Meng, X., Karniadakis, G.E.: B-pinns: Bayesian physics-informed neural networks for forward and inverse pde problems with noisy data. Journal of Computational Physics **425**, 109913 (2021)
- [7] Kharazmi, E., Zhang, Z., Karniadakis, G.E.: hp-vpinns: Variational physicsinformed neural networks with domain decomposition. Computer Methods in Applied Mechanics and Engineering 374, 113547 (2021)
- [8] Chiu, P.-H., Wong, J.C., Ooi, C., Dao, M.H., Ong, Y.-S.: Can-pinn: A fast physicsinformed neural network based on coupled-automatic-numerical differentiation

- method. Computer Methods in Applied Mechanics and Engineering **395**, 114909 (2022)
- [9] Zhu, Z., Hao, J., Huang, J., Huang, B.: Bc-pinn: an adaptive physics informed neural network based on biased multiobjective coevolutionary algorithm. Neural Computing and Applications 35(28), 21093–21113 (2023)
- [10] Su, C., Liang, J., He, Z.: E-pinn: A fast physics-informed neural network based on explicit time-domain method for dynamic response prediction of nonlinear structures. Engineering Structures **321**, 118900 (2024)
- [11] Khan, A., Lowther, D.A.: Physics informed neural networks for electromagnetic analysis. IEEE Transactions on Magnetics **58**(9), 1–4 (2022)
- [12] Beltrán-Pulido, A., Bilionis, I., Aliprantis, D.: Physics-informed neural networks for solving parametric magnetostatic problems. IEEE Transactions on Energy Conversion **37**(4), 2678–2689 (2022)
- [13] Baldan, M., Di Barba, P., Lowther, D.A.: Physics-informed neural networks for inverse electromagnetic problems. IEEE Transactions on Magnetics **59**(5), 1–5 (2023)
- [14] Lippert, J.R., Tresckow, M., De Gersem, H., Loukrezis, D.: Transfer learning-based physics-informed neural networks for magnetostatic field simulation with domain variations. International Journal of Numerical Modelling: Electronic Networks, Devices and Fields 37(4), 3264 (2024)
- [15] Cai, S., Wang, Z., Wang, S., Perdikaris, P., Karniadakis, G.E.: Physics-informed neural networks for heat transfer problems. Journal of Heat Transfer 143(6), 060801 (2021)
- [16] Cai, S., Mao, Z., Wang, Z., Yin, M., Karniadakis, G.E.: Physics-informed neural networks (pinns) for fluid mechanics: A review. Acta Mechanica Sinica 37(12), 1727–1738 (2021)
- [17] Eivazi, H., Tahani, M., Schlatter, P., Vinuesa, R.: Physics-informed neural networks for solving reynolds-averaged navier—stokes equations. Physics of Fluids **34**(7) (2022)
- [18] Zhao, C., Zhang, F., Lou, W., Wang, X., Yang, J.: A comprehensive review of advances in physics-informed neural networks and their applications in complex fluid dynamics. Physics of Fluids **36**(10) (2024)
- [19] Samaniego, E., Anitescu, C., Goswami, S., Nguyen-Thanh, V.M., Guo, H., Hamdia, K., Zhuang, X., Rabczuk, T.: An energy approach to the solution of partial differential equations in computational mechanics via machine learning: Concepts, implementation and applications. Computer Methods in Applied Mechanics and

- Engineering 362, 112790 (2020)
- [20] Bai, J., Rabczuk, T., Gupta, A., Alzubaidi, L., Gu, Y.: A physics-informed neural network technique based on a modified loss function for computational 2d and 3d solid mechanics. Computational Mechanics **71**(3), 543–562 (2023)
- [21] Linden, L., Klein, D.K., Kalina, K.A., Brummund, J., Weeger, O., Kästner, M.: Neural networks meet hyperelasticity: A guide to enforcing physics. Journal of the Mechanics and Physics of Solids **179**, 105363 (2023)
- [22] Hu, H., Qi, L., Chao, X.: Physics-informed neural networks (pinn) for computational solid mechanics: Numerical frameworks and applications. Thin-Walled Structures, 112495 (2024)
- [23] Markidis, S.: The old and the new: Can physics-informed deep-learning replace traditional linear solvers? Frontiers in big Data 4, 669097 (2021)
- [24] Grossmann, T.G., Komorowska, U.J., Latz, J., Schönlieb, C.-B.: Can physics-informed neural networks beat the finite element method? IMA Journal of Applied Mathematics 89(1), 143–174 (2024)
- [25] Hughes, T.J., Cottrell, J.A., Bazilevs, Y.: Isogeometric analysis: Cad, finite elements, nurbs, exact geometry and mesh refinement. Computer Methods in Applied Mechanics and Engineering 194(39-41), 4135–4195 (2005)
- [26] Cottrell, J.A., Hughes, T.J., Bazilevs, Y.: Isogeometric Analysis: Toward Integration of CAD and FEA. John Wiley & Sons, ??? (2009)
- [27] Nguyen, V.P., Anitescu, C., Bordas, S.P., Rabczuk, T.: Isogeometric analysis: an overview and computer implementation aspects. Mathematics and Computers in Simulation 117, 89–116 (2015)
- [28] Farhat, C., Roux, F.-X.: A method of finite element tearing and interconnecting and its parallel solution algorithm. International Journal for Numerical Methods in Engineering **32**(6), 1205–1227 (1991)
- [29] Kleiss, S.K., Pechstein, C., Jüttler, B., Tomar, S.: Ieti-isogeometric tearing and interconnecting. Computer Methods in Applied Mechanics and Engineering 247, 201–215 (2012)
- [30] Apostolatos, A., Schmidt, R., Wüchner, R., Bletzinger, K.-U.: A nitsche-type formulation and comparison of the most common domain decomposition methods in isogeometric analysis. International Journal for Numerical Methods in Engineering 97(7), 473–504 (2014)
- [31] Brivadis, E., Buffa, A., Wohlmuth, B., Wunderlich, L.: Isogeometric mortar methods. Computer Methods in Applied Mechanics and Engineering 284, 292–319

- [32] Merkel, M., Kapidani, B., Schöps, S., Vázquez, R.: Torque computation with the isogeometric mortar method for the simulation of electric machines. IEEE Transactions on Magnetics **58**(9), 1–4 (2022)
- [33] Khodayi-Mehr, R., Zavlanos, M.: Varnet: Variational neural networks for the solution of partial differential equations. In: Learning for Dynamics and Control, pp. 298–307 (2020). PMLR
- [34] Goswami, S., Anitescu, C., Chakraborty, S., Rabczuk, T.: Transfer learning enhanced physics informed neural network for phase-field modeling of fracture. Theoretical and Applied Fracture Mechanics 106, 102447 (2020)
- [35] Haghighat, E., Raissi, M., Moure, A., Gomez, H., Juanes, R.: A physics-informed deep learning framework for inversion and surrogate modeling in solid mechanics. Computer Methods in Applied Mechanics and Engineering 379, 113741 (2021)
- [36] Cao, G., Wang, X.: Parametric extended physics-informed neural networks for solid mechanics with complex mixed boundary conditions. Journal of the Mechanics and Physics of Solids 194, 105944 (2025)
- [37] von Tresckow, M., Kurz, S., De Gersem, H., Loukrezis, D.: A neural solver for variational problems on cad geometries with application to electric machine simulation. Journal of Machine Learning for Modeling and Computing **3**(1), 49–75 (2022)
- [38] Kostas, K.V., Politis, C.G., Zhanabay, I., Kaklis, P.D.: A physics-informed parametrization and its impact on 2d igabem analysis. Engineering with Computers, 1–20 (2024)
- [39] Möller, M., Toshniwal, D., Ruiten, F.: Physics-informed machine learning embedded into isogeometric analysis. Mathematics: key enabling technology for scientific machine learning. Platform Wiskunde, Amsterdam, 57–59 (2021)
- [40] Prasad, A.D., Balu, A., Shah, H., Sarkar, S., Hegde, C., Krishnamurthy, A.: Nurbs-diff: A differentiable programming module for nurbs. Computer-Aided Design 146, 103199 (2022)
- [41] Gasick, J., Qian, X.: Isogeometric neural networks: A new deep learning approach for solving parameterized partial differential equations. Computer Methods in Applied Mechanics and Engineering 405, 115839 (2023)
- [42] Nath, D., Neog, D.R., Gautam, S.S.: Transfer learning enhanced deep neural network application in gauss quadrature for isogeometric analysis. Engineering Applications of Artificial Intelligence **145**, 110182 (2025)

- [43] Saidaoui, H., Espath, L., Tempone, R.: Deep nurbs—admissible physics-informed neural networks. Engineering with Computers, 1–15 (2024)
- [44] Li, A., Zhang, Y.J.: Isogeometric analysis-based physics-informed graph neural network for studying traffic jam in neurons. Computer Methods in Applied Mechanics and Engineering 403, 115757 (2023)
- [45] Xu, G., Xie, J., Zhong, W., Toyoura, M., Ling, R., Xu, J., Gu, R., Wang, C.C., Rabczuk, T.: Iga-graph-net: Isogeometric analysis-reuse method based on graph neural networks for topology-consistent models. Journal of Computational Physics 521, 113544 (2025)
- [46] Wang, D., Xu, J., Gao, F., Wang, C.C., Gu, R., Lin, F., Rabczuk, T., Xu, G.: Iga-reuse-net: A deep-learning-based isogeometric analysis-reuse approach with topology-consistent parameterization. Computer Aided Geometric Design 95, 102087 (2022)
- [47] Lu, Y., Li, H., Zhang, L., Park, C., Mojumder, S., Knapik, S., Sang, Z., Tang, S., Apley, D.W., Wagner, G.J., et al.: Convolution hierarchical deep-learning neural networks (c-hidenn): finite elements, isogeometric analysis, tensor decomposition, and beyond. Computational Mechanics 72(2), 333–362 (2023)
- [48] Zhang, L., Park, C., Lu, Y., Li, H., Mojumder, S., Saha, S., Guo, J., Li, Y., Abbott, T., Wagner, G.J., et al.: Isogeometric convolution hierarchical deep-learning neural network: Isogeometric analysis with versatile adaptivity. Computer Methods in Applied Mechanics and Engineering 417, 116356 (2023)
- [49] Zhang, L., Park, C., Hughes, T.J., Liu, W.K.: Multi-patch isogeometric convolution hierarchical deep-learning neural network. Computer Methods in Applied Mechanics and Engineering 434, 117582 (2025)
- [50] Jagtap, A.D., Karniadakis, G.E.: Extended physics-informed neural networks (xpinns): A generalized space-time domain decomposition based deep learning framework for nonlinear partial differential equations. Communications in Computational Physics 28(5) (2020)
- [51] Jagtap, A.D., Kharazmi, E., Karniadakis, G.E.: Conservative physics-informed neural networks on discrete domains for conservation laws: Applications to forward and inverse problems. Computer Methods in Applied Mechanics and Engineering 365, 113028 (2020)
- [52] Zhang, B., Wu, G., Gu, Y., Wang, X., Wang, F.: Multi-domain physics-informed neural network for solving forward and inverse problems of steady-state heat conduction in multilayer media. Physics of Fluids **34**(11) (2022)
- [53] Sarma, A.K., Roy, S., Annavarapu, C., Roy, P., Jagannathan, S.: Interface pinns (i-pinns): A physics-informed neural networks framework for interface problems.

- Computer Methods in Applied Mechanics and Engineering 429, 117135 (2024)
- [54] Sukumar, N., Srivastava, A.: Exact imposition of boundary conditions with distance functions in physics-informed deep neural networks. Computer Methods in Applied Mechanics and Engineering 389, 114333 (2022)
- [55] Wang, J., Mo, Y., Izzuddin, B., Kim, C.-W.: Exact dirichlet boundary physicsinformed neural network epinn for solid mechanics. Computer Methods in Applied Mechanics and Engineering 414, 116184 (2023)
- [56] Luong, K.A., Le-Duc, T., Lee, S., Lee, J.: A novel normalized reduced-order physics-informed neural network for solving inverse problems. Engineering with Computers **40**(5), 3253–3272 (2024)
- [57] Le-Duc, T., Lee, S., Nguyen-Xuan, H., Lee, J.: A hierarchically normalized physics-informed neural network for solving differential equations: Application for solid mechanics problems. Engineering Applications of Artificial Intelligence 133, 108400 (2024)
- [58] Deguchi, S., Asai, M.: Dynamic & norm-based weights to normalize imbalance in back-propagated gradients of physics-informed neural networks. Journal of Physics Communications **7**(7), 075005 (2023)
- [59] Tresckow, M., De Gersem, H., Loukrezis, D.: Error approximation and bias correction in dynamic problems using a recurrent neural network/finite element hybrid model. Applied Mathematical Modelling 129, 428–447 (2024)
- [60] Xu, S., Dai, Y., Yan, C., Sun, Z., Huang, R., Guo, D., Yang, G.: On the preprocessing of physics-informed neural networks: how to better utilize data in fluid mechanics. Journal of Computational Physics, 113837 (2025)
- [61] Evans, L.C.: Partial Differential Equations vol. 19. American Mathematical Society, ??? (2022)
- [62] Bottou, L., et al.: Stochastic gradient learning in neural networks. Proceedings of Neuro-Nimes 91(8), 12 (1991)
- [63] Kingma, D.P., Ba, J.: Adam: a method for stochastic optimization. In: 3rd International Conference for Learning Representations, San Diego, pp. 1–10 (2015)
- [64] Piegl, L., Tiller, W.: The NURBS Book. Springer, ??? (2012)
- [65] Jackson, J.D.: Classical Electrodynamics. John Wiley & Sons, ??? (2021)
- [66] He, K., Zhang, X., Ren, S., Sun, J.: Deep residual learning for image recognition. In: Proceedings of the IEEE Conference on Computer Vision and Pattern Recognition, pp. 770–778 (2016)

- [67] Alnaes, M.S., Logg, A., Ølgaard, K.B., Rognes, M.E., Wells, G.N.: Unified form language: A domain-specific language for weak formulations of partial differential equations. ACM Transactions on Mathematical Software **40** (2014)
- [68] Logg, A., Wells, G.N.: Dolfin: Automated finite element computing. ACM Transactions on Mathematical Software 37 (2010) https://doi.org/10.1145/1731022. 1731030
- [69] Bonet, J., Gil, A.J., Wood, R.D.: Nonlinear Solid Mechanics for Finite Element Analysis: Dynamics. Cambridge University Press, ??? (2021)
- [70] Wriggers, P., Laursen, T.A.: Computational Contact Mechanics vol. 2. Springer, ??? (2006)
- [71] Dhondt, G.: The Finite Element Method for Three-Dimensional Thermomechanical Applications. John Wiley & Sons, ??? (2004)